HHS Public Access

Author manuscript

Org Biomol Chem. Author manuscript; available in PMC 2019 March 25.

Published in final edited form as:

Org Biomol Chem. 2017 June 21; 15(24): 5220–5226. doi:10.1039/c7ob00875a.

Balancing the intermolecular forces in peptide amphiphiles for controlling self-assembly transitions†

C. J. Buettner[a], **A. J. Wallace**[a], **S. Ok**[b], **A. A. Manos**[a], **M. J. Nicholl**[a], **A. Ghosh**[a], **M. F. Tweedle**[c], and **J. E. Goldberger**[a]

[a]Department of Chemistry and Biochemistry, The Ohio State University, Columbus, OH 43210, USA. goldberger.4@osu.edu

[b]School of Earth Sciences, The Ohio State University, Columbus, OH 43210, USA

[c]Department of Radiology, Wright Center for Innovation in Biomolecular Imaging, The Ohio State University, Columbus, Ohio 43210, USA

Abstract

While the influence of alkyl chain length and headgroup size on self-assembly behaviour has been well-established for simple surfactants, the rational control over the pH- and concentration-dependent self-assembly behaviour in stimuli responsive peptides remains an elusive goal. Here, we show that different amphiphilic peptides can have similar self-assembly phase diagrams, providing the relative strengths of the attractive and repulsive forces are balanced. Using palmitoyl-YYAAEEEEK(DO3A:Gd)-NH_2 and palmitoyl-YAAEEEEK(DO3A:Gd)-NH_2 as controls, we show that reducing hydrophobic attractive forces through fewer methylene groups in the alkyl chain will lead to a similar self-assembly phase diagram as increasing the electrostatic repulsive forces *via* the addition of a glutamic acid residue. These changes allow creation of self-assembled MRI vehicles with slightly different micelle and nanofiber diameters but with minimal changes in the spin–lattice T_1 relaxivity. These findings reveal a powerful strategy to design self-assembled vehicles with different sizes but with similar self-assembly profiles.

Introduction

Creating stimuli responsive materials that undergo morphological transitions *in vivo* for next generation sensing, diagnostic and therapeutic agents requires the design of molecules with well-tailored self-assembly transitions.[1–8] For example, developing vehicles that change into different sizes and shapes in healthy and diseased tissue will enable new vehicles that exploit differences in diffusion kinetics for enhanced accumulation at a disease site.[9] For simple surfactant molecules, the relative influence of the electrostatic repulsion of the head group and the attractive forces in the alkyl chain length on their morphology and critical aggregation concentrations has been established.[10] However, the rational design of biocompatible transitioning vehicles comprised of drugs, imaging moieties, biological building blocks, and other stimuli responsive elements with similar self-assembly behaviour but different sizes remains elusive.

†Electronic supplementary information (ESI) available. See DOI: 10.1039/c7ob00875a

Previously, we have developed a class of peptide based surfactants that undergoes a pH-triggered self-assembly transition from micelles in more basic conditions, to nanofibers in more acidic conditions. The pH-trigger varies between 7.4 (physiological pH) and 6.6 (extracellular pH of many cancerous tumours) in order to enhance the accumulation of these vehicles locally in a tumour when systemically administered.[11–15] Typically, the design of these peptide amphiphiles (PAs) feature a palmitoyl tail, a 4-amino acid β-sheet region consisting of one strongly hydrophobic amino acid and three alanine residues, four glutamic acids, and a lysine coupled to 1,4,7-tris [carboxymethylaza]cylododecane-10-azaacetyl amide (DO3A) for Gd^{3+} incorporation[11] (Chart 1). The hydrophobic region (β-sheet region) promotes nanofiber formation, while the anionic charged region destabilizes these structures *via* electrostatic repulsion, leading to the formation of micelles. In balancing these forces within the PAs, we have shown that the pH of self-assembly can be tuned based on the β-sheet propensity of the hydrophobic amino acid,[11] and the isomerization of the peptide sequence.[14] Both are important avenues for developing biomaterials that undergo self-assembly transitions at precise pH values.

We now look to understand how balancing the attractive forces of the peptide amphiphile *via* the alkyl chain length influences pH- and concentration-dependent self-assembly behaviour, to create differently sized transitioning vehicles that undergo self-assembly transitions at similar pH values. The ability to fine tune the hydrodynamic diameter will enable further control of the diffusion kinetics into the tumor microenvironment, and tissue distribution properties *in vivo*.[16] In general, smaller vehicles tend to have larger diffusion coefficients, and consequently, have more rapid entry into the tumor. However, vehicles with rigid cores that are below ~10 nm in diameter are excreted through the glomerular filtration system of the kidney more efficiently than larger entities.[17–20] Thus, control over the vehicle size allows optimal efficacy *via* maximizing tumour entry and minimizing excretion loss. These self-assembling vehicles are expect to have much longer blood clearance half-lifes compared to small molecule Gd-chelates. Furthermore, MRI-contrast agents that are rigidly bound to larger, more slowly rotating vehicles exhibit greater spin–lattice relaxation times (T_1).[21]

In this article, we establish a general relationship between the alkyl chain length, number of strongly hydrophobic amino acids, and the number of anionic amino acids in the PA sequence with the pH- and concentration-dependent self-assembly behaviour. This was accomplished by synthesizing and comparing palmitoyl-YYAAEEEEEK(DO3A:Gd)-NH_2 and pentadecyl-YYAAEEEEK(DO3A:Gd)-NH_2 to palmitoyl-YYAAEEEEK(DO3A: Gd)-NH_2, as well as palmitoyl-YAAAEEEEEK(DO3A:Gd)-NH_2 and pentadecyl-YAAAEEEEK(DO3A:Gd)-NH_2 to palmitoyl-YAAAEEEEK(DO3A:Gd)-NH_2 (Table 1). In other words, compared to PA1, PA2 has one additional glutamic acid residue and PA3 has one less $-CH_2-$ group in the alkyl chain. PA5 and PA6 have similar changes, respectively, in comparison to PA4. We show that either decreasing the attractive forces by removing a single $-CH_2-$ unit or increasing the repulsive forces by adding a single glutamic acid disrupts nanofiber formation, and thus, the critical aggregation concentrations (CAC) increase and the micelle-to-nanofiber transition pHs occur at more acidic values.

Materials and methods

Materials

All PAs were prepared using solid phase Fmoc peptide synthesis with amino acids purchased from ChemImpex. All PAs were purified *via* reverse-phase high-performance liquid chromatography (HPLC), dialyzed to remove salts and lyopholized. HPLC and electrospray ionization mass spectrometry (ESI-MS) were used to assess the purity and identity of the PAs (SI-1,2†). The full synthesis of PAs can be found in the ESI Methods.†

Circular dichroism

Circular Dichroism (CD) was used to determine the pH-dependent morphologies of the PAs. All samples were basified to a pH of 10, stirred at 90 °C for 30 minutes in an oil bath and cooled to room temperature over a span of 2–6 hours to ensure the molecule was not in a kinetically trapped state after lyophilization. CD measurements were carried out on a JASCO J-815 Spectrometer using 0.1–1 cm path length quartz cuvettes with PA concentrations ranging from 10 μM to 500 μM in a salt solution consisting of 150 mM NaCl and 2.2 mM $CaCl_2$.[13] Aqueous HCl and NaOH solutions were added to adjust the pH of the PA solution, which was measured with an Accumet XL15 pH meter (Fisher Scientific), along with an Orion Ross Ultra semimicro electrode (8103BNUWP, Thermo Scientific). Three accumulations were measured at a wavelength range of 260–190 nm at a scanning speed of 100 nm min^{-1} with an integration time of 2 or 4 seconds for each data series. Representative CD-curves at Fig. SI-3† were chosen from measurements collected at 50 μM PA, as this concentration features the highest signal-to-noise while showing a transition.

A β-sheet CD curve was defined as one that featured a local minimum at 218–220 nm The pH at which the micelle/single molecule to nanofiber transition occurs was defined as the midpoint pH between the lowest pH random coil pattern (no minimum at 218–220 nm) and the highest pH β-sheet curve.

Critical aggregation concentration measurements

CAC measurements were carried out to determine the concentration at which micelles or nanofibers begin to form, using the pyrene 1 : 3 method.[22] When the PAs form an assembled structure with a hydrophobic pocket capable of encapsulating pyrene (micelles or nanofibers), the intensity ratio of pyrene fluorescence at 376 and 392 nm changes. All samples were basified to a pH of 10, stirred at 90 °C for 30 minutes in an oil bath and cooled to room temperature over a span of 2–6 hours. HCl and NaOH were then added to set the PA solution to specific pH values. PAs with concentrations ranging from 100 to 500 μM were serially diluted with 150 mM NaCl and 2.2 mM $CaCl_2$. A pyrene solution was then added to each of the diluted samples, for a final pyrene concentration of 4.5 μM. 100 μL of each serially diluted sample was transferred into a 96-well plate and the fluorescence emission of the pyrene was monitored by a hybrid reader fluorimeter (BioTek Synergy H4) at room temperature with an excitation wavelength of 335 nm. The pyrene fluorescence was

†Electronic supplementary information (ESI) available. See DOI: 10.1039/c7ob00875a

monitored from 360 to 430 nm, and the intensity of the emission peaks at 376 and 392 nm were compared at different concentrations to determine the CAC for each pH.

Transmission electron microscopy (TEM)

Transmission electron microscopy was employed to confirm the self-assembled morphology at different pH values and concentrations. The sample to be tested was basified to a pH of 10, stirred at 90 °C in an oil bath for 30 minutes and cooled to room temperature over a span of 2–6 hours. The pH was then adjusted with HCl and NaOH to set the peptide solution that was dissolved in 150 mM NaCl and 2.2 mM $CaCl_2$ to a pH of either 5 or 9. Once the desired pH was reached, 5 μL of the solution was spread onto a Carbon Formvar and allowed to sit for one minute before being wicked dry with filter paper. A 1 wt% uranyl acetate solution was added and spread over the grid to negatively stain the sample, and was wicked dry immediately after application. The grid was then examined using a FEI Tecnai G2 Biotwin TEM at 100 keV. The diameters of each self-assembled morphology were determined *via* averaging at least 30 different objects.

T_1 measurements

T_1 relaxation time measurements were carried out with various concentrations of the PAs dissolved in 150 mM NaCl and 2.2 mM $CaCl_2$ solutions at multiple pH values on a benchtop minispec mq20 (NF series, Bruker, Germany). It uses a permanent magnet to create a field (0.469 T) corresponding to a proton resonance frequency of 19.95 MHz. The sample temperature was kept at 40 °C. For all samples, the magnetic field was matched to the resonance circuit, and the durations were on the order of 2.8 and 5.6 μs at full amplitude for π/2- and π-pulses, respectively. The inversion–recovery pulse sequence was used to measure the ^1H T_1 relaxation times in the laboratory frame. In this pulse sequence, a 180° radio frequency pulse was used to invert the bulk magnetization, which was then allowed to recover to equilibrium *via* the T_1 relaxation process over a variable recovery time, before acquisition of the free-induction decay with 32 data points and 16 scans per point. A recycle delay time of 5 T_1 was used to allow the system to fully relax between FID acquisitions, and phase cycling was employed to eliminate signal artifacts. Relaxivity (r_1) values were then obtained from the slopes of $1/T_1$ *vs.* [PA-Gd(DO3A)] plots using the following equation:

$$\frac{1}{T_1} = \frac{1}{T_{1,\mathrm{d}}} + r_1[\mathrm{PA}] \quad (1)$$

where $T_{1,\mathrm{d}}$ refers to the water proton relaxation time in the absence of the peptide contrast agent. Eq (1)

DLS measurements

For DLS measurements, PAs were dissolved in 150 mM NaCl, 2.2 mM $CaCl_2$ in deionized water and filtered with 250 nm filters. The solutions were basified to a pH of 10, stirred at 90 °C in an oil bath for 30 minutes and cooled to room temperature overnight. The solutions were bath sonicated and then adjusted to the appropriate concentrations and pH values such

that they exhibited a micelle morphology (50 μM and pH = 10.5). DLS measurements were performed using a Malvern Nano series Zetasizer.

Results and discussion

Self-assembly behaviour

PA1, which features a palmitoyl alkyl tail, two β-sheet forming tyrosine residues, and four glutamic acids, has the strongest attractive forces and weakest repulsive forces of the PAs in this study. The CD of PA1 at 10 μM, which corresponds to a concentration close to the limit of detection for our CD instrument, for pH values ranging from 5–11 reveals a β-sheet pattern, indicative of nanofiber formation (Fig. 1a). The nanofiber morphology was confirmed by TEM of samples prepared at pH values of 5 and 9 at 500 μM (Fig. 1b and c). The diameters of the nanofibers at pH 5 and 9 were observed to be 8.5 ± 1.0 nm and 8.6 ± 0.9 nm, respectively, with no statistically significant difference, as expected. Therefore, across all pH and concentration values within our limits of detection, PA1 is assembled in the nanofiber morphology.

In order to induce a micelle-to-nanofiber transition in this pH range, PA2, having increased repulsive forces *via* the addition of a fifth glutamic acid, and PA3, having decreased attractive forces through the shortening of the alkyl chain length, were synthesized. Fig. 2a shows the CD of PA2 at 50 μM, which undergoes a pH-dependent morphology transition from either isolated molecules or micelles at basic pH values to nanofibers below a pH of 5.75.

To distinguish if PA2 exists as isolated molecules or is assembled into micelles, the CAC was determined at different pH values (Fig. 2b). For instance, the CAC values at pH values of 7.06 and 9.02 were extrapolated to be 9.3 and 21.6 μM, respectively. At more acidic pH values of pH 6 and pH 5, the CAC values for PA2 drop to 5.6 μM and below the detectable limit of 1 μM. The phenolic tyrosine residue, which has a pK_a of ~10.5 when free, will also contribute to the increase in CAC at more basic values. The pH-dependent CD and concentration-dependent CAC were also collected for PA3 (Fig. SI-3†). Again, a pH-dependent morphological transition from isolated molecules/micelles at basic pH values to nanofibers at acidic pH values, as well as an increase in CAC at more basic pH values were observed.

In order to distinguish whether adding a fifth glutamic acid or reducing the alkyl chain length had a greater effect on disrupting nanofiber formation, the concentration-dependent CD and pH-dependent CAC measurements were combined to construct the pH *vs.* concentration self-assembly phase diagrams for both PA2 and PA3 (Fig. 3a). At high concentrations and low pH values, the PAs assemble into nanofibers. At high pH values and intermediate concentrations the PAs assemble into micelles, and at concentrations below the CAC values, the PA remains in the unassembled molecular state. The self-assembly phase diagrams for PA2 and PA3 were relatively similar, however, PA3 had a greater propensity to form nanofibers at a given concentration than PA2. At all concentrations observed, PA3 transitions from micelles to nanofibers at only 0.15–0.63 pH units more basic than PA2. Additionally, at all pH values except at pH 9, the CAC measurements for PA2 were typically

higher than PA3. This shows that increasing repulsive forces from the addition of a glutamic acid has a greater effect on disrupting nanofiber formation than decreasing the attractive forces by shortening the alkyl tail by one methylene unit. TEM further confirms the micelle and nanofiber morphology of PA2 and PA3 at various concentrations and pH values (Fig. 3b–e). The diameters of the nanofibers for PA2 and PA3 were observed to be 9.7 ± 1.2 nm and 8.1 ± 1.3 nm, respectively. The differences in these nanofiber diameters are consistent with the expected changes for cylindrical nanofibers consisting of hydrophobically collapsed β-sheets featuring a single PA molecule radius. For instance the diameter of PA1 from TEM measurements is ~0.4 nm larger than PA3, which is close to the ~0.3 nm difference that is expected from the addition of 2 $-CH_2-$ units per diameter. The nanofiber diameter of PA2 is 1.2 nm larger than PA1, which also fits the expectation of the addition of a glutamic acid residue. Furthermore, the micelles formed by PA2 and PA3 had observed hydrodynamic diameters of 11.3 ± 1.5 nm and 10.8 ± 1.6 nm, respectively from DLS measurements (Fig. 4). The size of the nanofiber does not determine the pH of transition, allowing independent control over both of these parameters using molecular design.

To demonstrate that this is a general trend we synthesized PAs 4, 5, and 6 which feature only a single tyrosine in the hydrophobic portion (YAAA), but have the same alkyl chain lengths and number of glutamic acids as PAs 1, 2, and 3, respectively. The same relative influence of number of hydrophobic amino acids and glutamic acids was observed. Since PA4 only has a single strongly hydrophobic tyrosine residue, transitions to both spherical micelles and the isolated molecule states were observed in the phase diagram (Fig. 5), in contrast to PA1. In PAs 4–6, the CACs were observed to be 7.3–15.5 μM from pH 5–9. Additionally, a strong concentration dependence in the micelle-to-nanofiber transition pH is apparent. PA5 contained one additional glutamic acid residue compared to PA4 (same difference as between PA2 and PA1). The pH of transition shifts to a more acidic pH value by ~0.2 units at lower concentrations and does not exhibit the strong concentration dependence until above 100 μM, giving it a much larger range of concentration and pH conditions in which it is in the micelle morphology. This results from the additional repulsive forces in PA5 that prevent the collapse into the nanofiber morphology. The additional repulsive force also leads to an increase in the CAC by 1–3 μM. This difference becomes less pronounced at more acidic pH values.

PA6 has one fewer $-CH_2-$ group compared to PA4 (same difference as PA3 and PA1). As previously seen the deletion of a methylene group has a less pronounced effect on the overall phase diagram of the PA. The pH of transition for PA6 is almost identical to PA4 and shows a very similar concentration dependent profile. The concentration dependence does occur at a concentration ~5–10 μM higher, indicating that PA6 can exist as a micelle at higher concentrations, as a result of having weaker attractive forces.

The CAC values of PA2–3 are lower than those of PAs 4–6 at acidic pH values, and are higher under basic pH values. One would expect that PAs with two strongly hydrophobic, beta-sheet forming residues (as in PA2 and PA3) would have a lower CAC, compared to PAs with one such reside (PAs 4–6). Indeed, at acidic pH values (pH < 7) PA2 and PA3, which feature two strongly hydrophobic tyrosine residues, have much lower CAC values compared to PAs 4–6. It is important to note that tyrosine residues are ionizable with a typical phenolic

pK_a of ~10. Therefore, more basic pH values lead to greater degrees of tyrosine deprotonation and more electrostatic repulsion between PA molecules, ultimately increasing the CAC. This explains why PA2 and PA3 have a higher CAC at more basic pH values compared to PA4–6.

Water T_1 relaxivity

In MRI imaging, a paramagnetic contrast agent accelerates the relaxivity of water. The concentration dependent relaxivity of all PAs were measured at pH values of 5.2 and 7.0. Since PAs 2–5 exhibit a concentration dependent transition from spherical micelles to nanofibers, at pH 7.0, the relaxivity was measured both at concentrations in the nanofiber state and in the micelle state and the relaxivity values were extracted separately. For all PAs the T_1 relaxivity typically ranges between 4.9–7.6 mM^{-1} s^{-1} while in the micelle morphology (Table 2). When the PAs are assembled in the nanofiber state either at lower pH values or at higher concentrations there is a marked increase in the T_1 relaxivity value to 8.5–10.5 mM^{-1} s^{-1}.

This increase in T_1 relaxivity in the nanofiber state is expected, as it is typically observed that tethering Gd^{3+} to larger, less-quickly rotating structures will lead to an increase in the relaxivity.[23] However, the small variations in the PA diameters for both the nanofiber and micelle morphologies that occurred by either subtracting a methylene group or adding a glutamic acid did not significantly affect the relaxivity. For example PA5, which has an additional glutamic acid and consequently a 1.2 and 1.6 nm larger nanofiber diameter compared to PAs 4 and 6, respectively, actually exhibits a slightly smaller relaxivity (8.6 mM^{-1} s^{-1}) than these PAs. This indicates that other factors are impacting the relaxivity, including the fiber rigidity and accessibility of H_2O to the Gd^{3+} paramagnetic centers.[24,25] For instance, it is possible that the additional glutamic acid in PA 5, causes the chelate to rotate more freely and more independently of the larger fiber, than in PA 6. Overall, the r_1 relaxivity of these PAs in both the nanofiber and micelle states remains higher than those of commercially available gadolinium chelates (3–4.5 mM^{-1} s^{-1} at 0.47 T).[26] The r_1 relaxivities for these commerical agents varies by at most 15% at a field strength of 0.47 to 4.7 T.[27]

Conclusions

Designing pH-triggered self-assembling vehicles that both undergo morphological transitions under precise sets of solution conditions as well as having controllable sizes for dictating biodistribution behaviour and clearance mechanisms is crucial to guarantee their functionality *in vivo*. This work shows that balancing the attractive and repulsive forces of peptide amphiphiles by changing the alkyl chain length and number of charged amino acid residues, respectively, allows self-assembly behaviour to be very similar for vehicles with varying sizes. For example, PA2 and PA3 have virtually identical pH- and concentration-dependent self-assembly behaviour, however, the nanofiber diameters vary by ~1.6 nm or almost 20%. This work will enable future explorations comparing the biodistribution of various sized Gd-labelled PA vehicles that transform from spherical micelles in the

bloodstream into nanofibers in the acidic cancer microenvironment, in order to design MRI-agents with maximum accumulation in tumour tissue.

Supplementary Material

Refer to Web version on PubMed Central for supplementary material.

Acknowledgements

The relaxivity measurements were generated using the facilities at the Subsurface Energy Materials Characterization & Analysis Laboratory at The Ohio State University. TEM images presented in this article were generated using the instruments and services at the Campus Microscopy and Imaging Facility at The Ohio State University. J. E. G. and M. F. T. graciously acknowledge the OSU Drug Discovery Institute, part of the Comprehensive Cancer Center, funded by the National Cancer Institute, Grant number, P30CA016058. M. F. T. acknowledges The Stefanie Spielman Foundation.

References

1. Schaefer C, Voets I, Palmans A, Meijer E, van der Schoot P and Besenius P, Controlling the cooperativity in the supramolecular polymerization of ionic discotic amphiphiles via electrostatic screening, ACS Macro Lett, 2012, 1, 830–833.
2. Besenius P, Heynens JL, Straathof R, Nieuwenhuizen MM, Bomans PH, Terreno E, Aime S, Strijkers GJ, Nicolay K and Meijer E, Paramagnetic self-assembled nanoparticles as supramolecular MRI contrast agents, Contrast Media Mol. Imaging, 2012, 7, 356–361. [PubMed: 22539406]
3. Cheetham AG, Zhang P, Lin Y.-a., Lock LL and Cui H, Supramolecular nanostructures formed by anticancer drug assembly, J. Am. Chem. Soc, 2013, 135, 2907. [PubMed: 23379791]
4. Zhao T, Huang G, Li Y, Yang S, Ramezani S, Lin Z, Wang Y, Ma X, Zeng Z and Luo M, A transistor-like pH nanoprobe for tumour detection and image-guided surgery, Nat. Biomed. Eng, 2016, 1, 0006. [PubMed: 28966871]
5. Cheetham AG, Lin Y.-a., Lin R and Cui H, Molecular design and synthesis of self-assembling camptothecin drug amphiphiles, Acta Pharmacol. Sin, 2017, 38, 874–884. [PubMed: 28260797]
6. Callmann CE, Barback CV, Thompson MP, Hall DJ, Mattrey RF and Gianneschi NC, Therapeutic Enzyme-Responsive Nanoparticles for Targeted Delivery and Accumulation in Tumors, Adv. Mater, 2015, 27, 4611–4615. [PubMed: 26178920]
7. Cui H, Cheetham AG, Pashuck ET and Stupp SI, Amino acid sequence in constitutionally isomeric tetrapeptide amphiphiles dictates architecture of one-dimensional nanostructures, J. Am. Chem. Soc, 2014, 136, 12461–12468. [PubMed: 25144245]
8. Appel R, Tacke S, Klingauf J and Besenius P, Tuning the pH-triggered self-assembly of dendritic peptide amphiphiles using fluorinated side chains, Org. Biomol. Chem, 2015, 13, 1030–1039. [PubMed: 25410414]
9. Chien M-P, Thompson MP, Lin EC and Gianneschi NC, Fluorogenic enzyme-responsive micellar nanoparticles, Chem. Sci, 2012, 3, 2690–2694. [PubMed: 23585924]
10. Israelachvili JN, Intermolecular and Surface Forces, Academic press, San Diego, 2011.
11. Ghosh A, Haverick M, Stump K, Yang X, Tweedle MF and Goldberger JE, Fine-tuning the pH trigger of self-assembly, J. Am. Chem. Soc, 2012, 134, 3647–3650. [PubMed: 22309293]
12. Cote Y, Fu IW, Dobson ET, Goldberger JE, Nguyen HD and Shen JK, Mechanism of the pH-controlled self-assembly of nanofibers from peptide amphiphiles, J. Phys. Chem, 2014, 118, 16272.
13. Ghosh A, Buettner CJ, Manos AA, Wallace AJ, Tweedle MF and Goldberger JE, Probing Peptide Amphiphile Self-Assembly in Blood Serum, Biomacromolecules, 2014, 15, 4488–4494. [PubMed: 25347387]
14. Ghosh A, Dobson ET, Buettner CJ, Nicholl MJ and Goldberger JE, Programming pH-Triggered Self-Assembly Transitions via Isomerization of Peptide Sequence, Langmuir, 2014, 30, 15383–15387. [PubMed: 25474500]

15. Goldberger JE and Tweedle MF, US Pat., 2014/0363378, 2014.
16. Lee ES, Gao Z and Bae YH, Recent progress in tumor pH targeting nanotechnology, J. Controlled Release, 2008, 132, 164–170.
17. Sun X, Rossin R, Turner JL, Becker ML, Joralemon MJ, Welch MJ and Wooley KL, An assessment of the effects of shell cross-linked nanoparticle size, core composition, and surface PEGylation on in vivo biodistribution, Biomacromolecules, 2005, 6, 2541–2554. [PubMed: 16153091]
18. Albanese A, Tang PS and Chan WC, The effect of nanoparticle size, shape, and surface chemistry on biological systems, Annu. Rev. Biomed. Eng, 2012, 14, 1–16. [PubMed: 22524388]
19. Choi CHJ, Zuckerman JE, Webster P and Davis ME, Targeting kidney mesangium by nanoparticles of defined size, Proc. Natl. Acad. Sci. U. S. A, 2011, 108, 6656–6661. [PubMed: 21464325]
20. Choi HS, Liu W, Misra P, Tanaka E, Zimmer JP, Ipe BI, Bawendi MG and Frangioni JV, Renal clearance of quantum dots, Nat. Biotechnol, 2007, 25, 1165–1170. [PubMed: 17891134]
21. Botta M and Tei L, Relaxivity Enhancement in Macromolecular and Nanosized GdIII-Based MRI Contrast Agents, Eur. J. Inorg. Chem, 2012, 2012, 1945–1960.
22. Aguiar J, Carpena P, Molina-Bolívar J and Ruiz CC, On the determination of the critical micelle concentration by the pyrene 1 : 3 ratio method, J. Colloid Interface Sci, 2003, 258, 116–122.
23. Yang JJ, Yang J, Wei L, Zurkiya O, Yang W, Li S, Zou J, Zhou Y, Maniccia ALW and Mao H, Rational design of protein-based MRI contrast agents, J. Am. Chem. Soc, 2008, 130, 9260–9267. [PubMed: 18576649]
24. Nicolle GM, Tóth É, Schmitt-Willich H, Radüchel B and Merbach AE, The impact of rigidity and water exchange on the relaxivity of a dendritic MRI contrast agent, Chem. – Eur. J, 2002, 8, 1040–1048. [PubMed: 11891890]
25. Werner EJ, Datta A, Jocher CJ and Raymond KN, High-Relaxivity MRI Contrast Agents: Where Coordination Chemistry Meets Medical Imaging, Angew. Chem., Int. Ed, 2008, 47, 8568–8580.
26. Hao D, Ai T, Goerner F, Hu X, Runge VM and Tweedle M, MRI contrast agents: basic chemistry and safety, J. Magn. Reson. Imaging, 2012, 36, 1060–1071. [PubMed: 23090917]
27. Rohrer M, Bauer H, Mintorovitch J, Requardt M and Weinmann HJ, Comparison of Magnetic Properties of MRI Contrast Media Solutions at Different Magnetic Field Strengths, Invest. Radiol, 2005, 40, 715–724. [PubMed: 16230904]

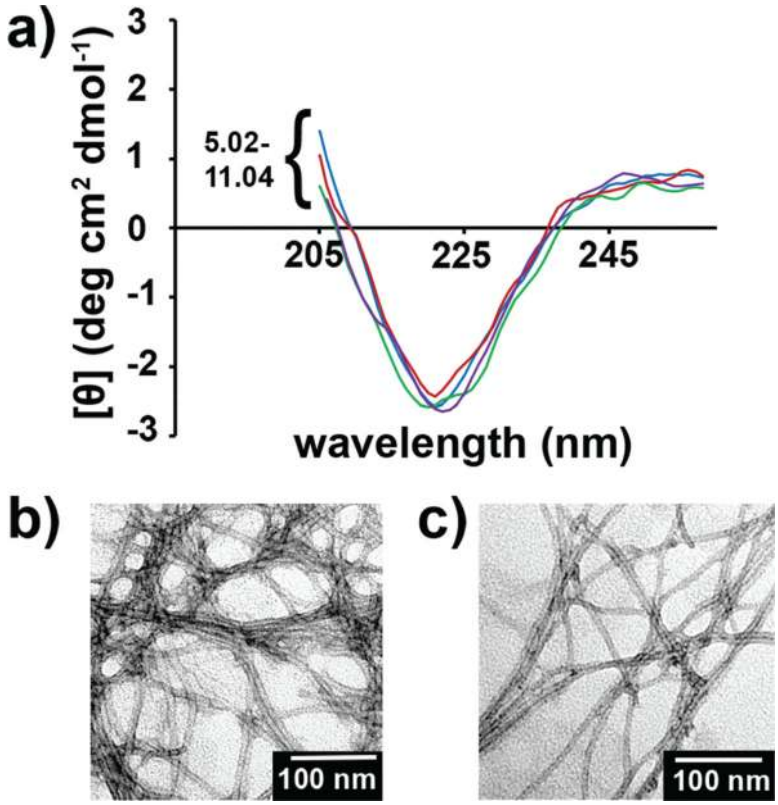

Fig. 1.

(a) CD trace of 10 μM PA1 showing β-sheet nanofiber morphology at pH values ranging from 5.02–11.04. (b, c) TEM of 500 μM solutions of PA 1 at (b) pH = 5 and (c) pH = 9. In both CD and TEM, the PA was dissolved in 150 mM NaCl and 2.2 mM $CaCl_2$.

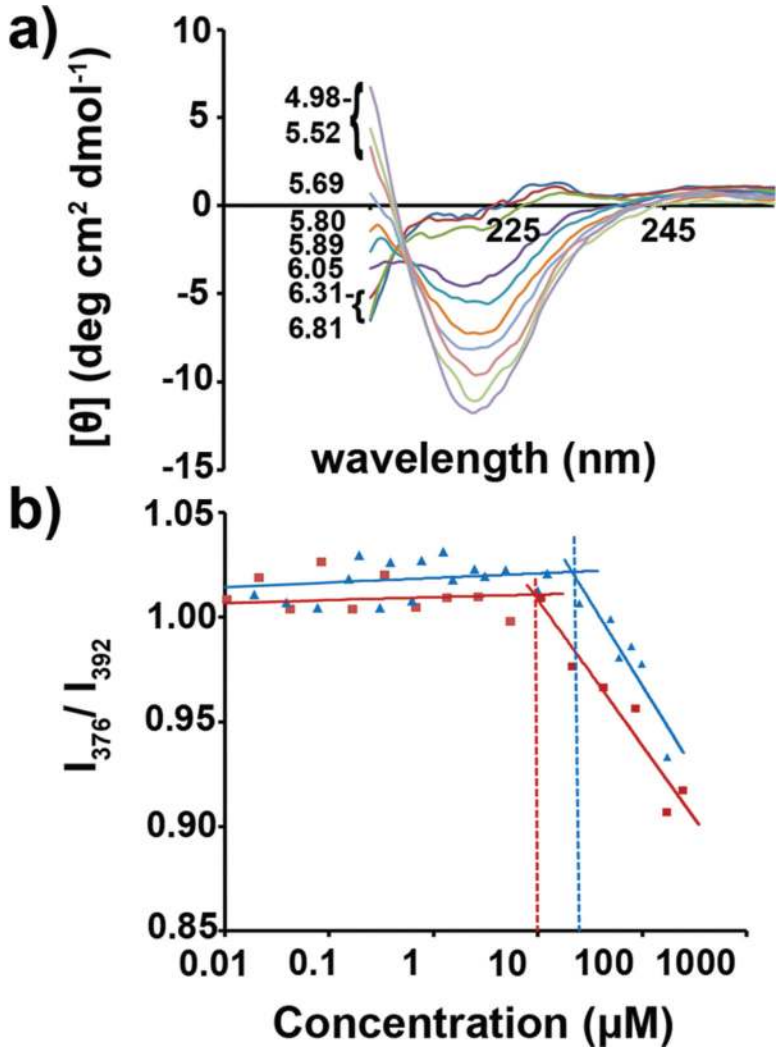

Fig. 2.

(a) CD of PA2 at 50 μM dissolved in 150 mM NaCl, and 2.2 mM $CaCl_2$ at various pH values showing a transition at a pH of 5.75. (b) Ratio of pyrene luminescence at 376 *vs.* 392 nm for PA2 at pH 7.06 (red) and pH 9.02 (blue). The dotted lines correspond to the CAC at these pH values.

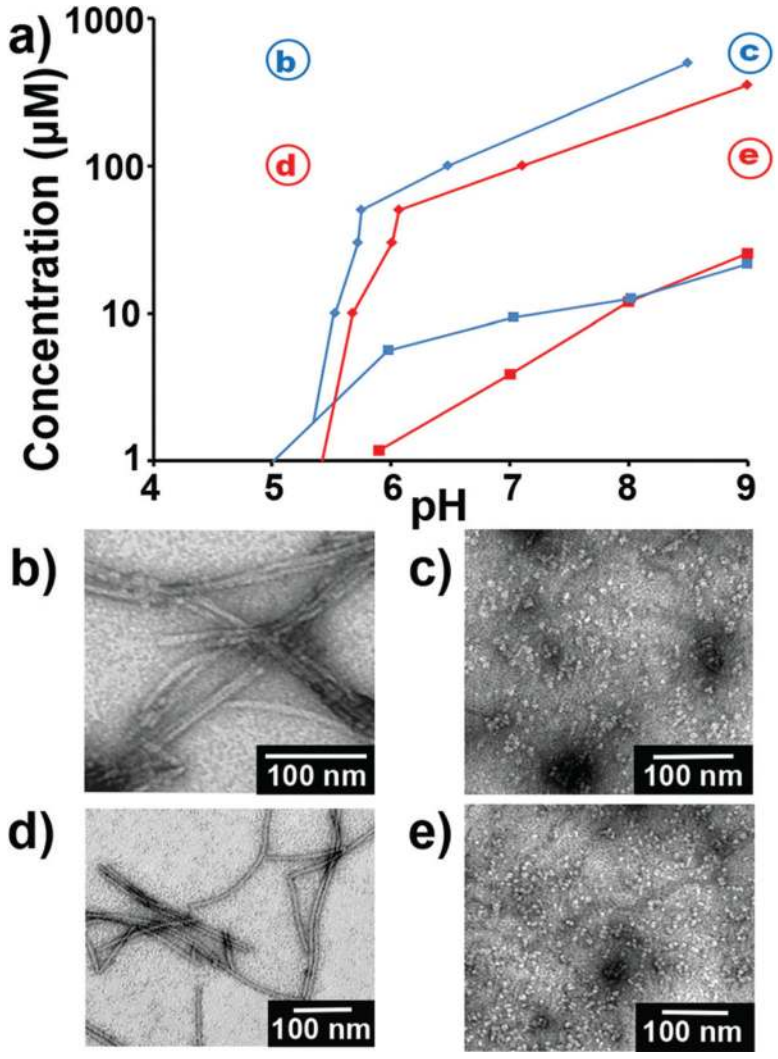

Fig. 3.

(a) Concentration-pH phase diagrams of PA2 (blue) and PA3 (red) determined by CD (diamonds) and CAC (squares). (b–e) TEM images of PAs: 500 μM PA2 at (b) pH 5 (c) pH 9 and 100 μM PA3 at (d) pH 5 and (e) pH 9. All measurements were performed in 150 mM NaCl and 2.2 mM $CaCl_2$.

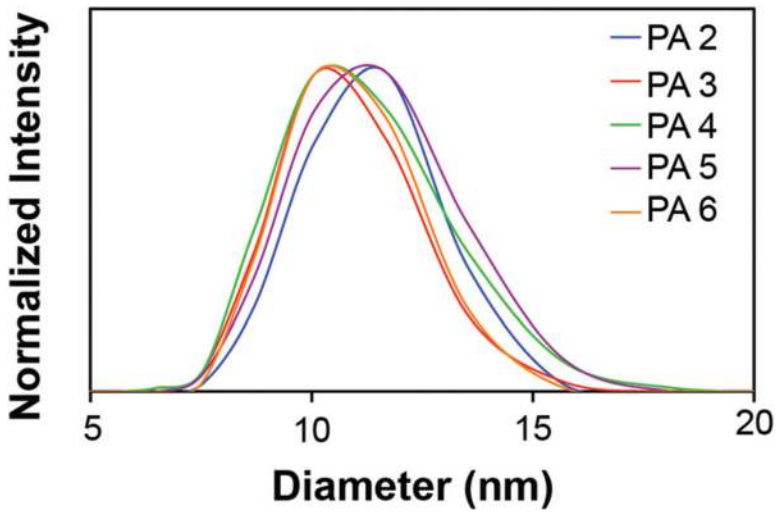

Fig. 4.

DLS trace of 100 μM solution of PAs 2–6, dissolved in 150 mM NaCl and 2.2 mM $CaCl_2$, at pH = 9.0.

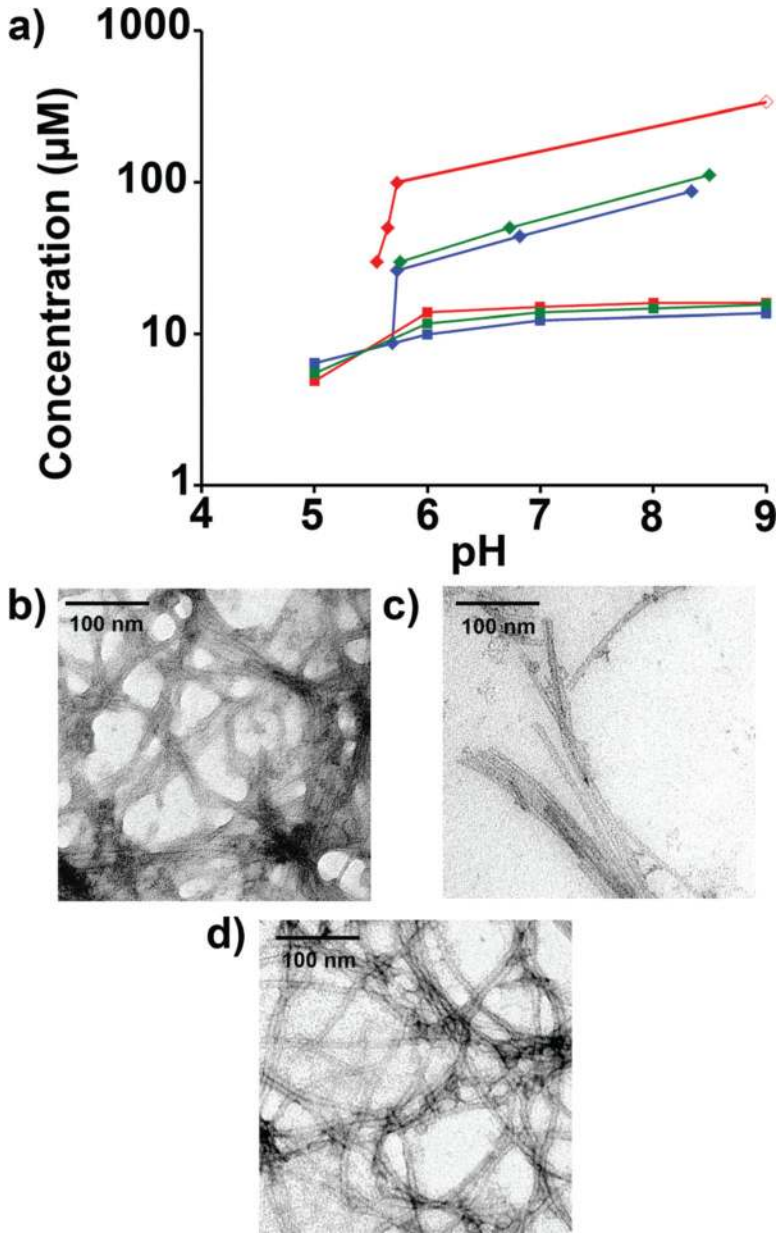

Fig. 5.

(a) pH- and concentration-dependent phase diagram of PA 4 (blue) PA 5 (red) and PA 6 (green). (b–d) TEM of 500 μM solutions of PA 4, 5, 6 respectively, at pH 5, in a solution of 150 mM NaCl and 2.2 mM $CaCl_2$.

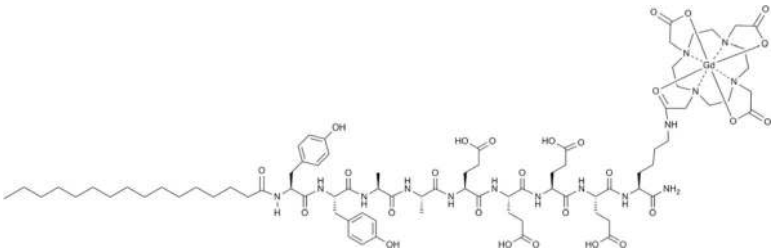

Chart 1.
Structure of PA1, palmitoyl-YYAAEEEEK(DO3A:Gd)-NH_2.

Table 1

Peptide sequence of PAs

MoIecuIe	Sequence
PA1	paImitoyI-YYAAEEEEK(DO3A:Gd)-NH_2
PA2	paImitoyI-YYAAEEEEEK(DO3A:Gd)-NH_2
PA3	pentadecyI-YYAAEEEEK(DO3A:Gd)-NH_2
PA4	paImitoyI-YAAAEEEEK(DO3A:Gd)-NH_2
PA5	paImitoyI-YAAAEEEEEK(DO3A:Gd)-NH_2
PA6	pentadecyI-YAAAEEEEK(DO3A:Gd)-NH_2

Table 2

Diameters and r_1 relaxivity for all PAs

Molecule	Micelle hydrodynamic diameter DLS (nm)	Nanofiber diameter TEM (nm)	r_1 micelle pH 7.0 (mM^{-1} s^{-1})	r_1 nanofiber pH 7.0 ($_{(mM^{-1}\ s^{-1})}$)	r_1 nanofiber pH 5.2 ($_{(mM^{-1}\ s^{-1})}$)
PA1	NA	8.5 ± 1.0	NA	10.6	10.5
PA2	11.3 ± 1.5	9.7 ± 1.2	4.9	10.0	10.2
PA3	10.8 ± 1.6	8.1 ± 1.3	5.1	8.4	9.5
PA4	11.0 ± 1.9	8.4 ± 1.4	7.6	9.3	10.2
PA5	11.2 ± 1.8	9.7 ± 0.8	5.7	8.6	8.5
PA6	10.8 ± 1.5	8.1 ± 0.9	6.5	9.1	9.6